CHAPTER 21

Quantitative Fluorescence Lifetime Imaging in Cells as a Tool to Design Computational Models of Ran-Regulated Reaction Networks

Petr Kalab* **and Arnd Pralle*,†**

*Department of Cell Biology
University of California
Berkeley, California 94720

†Department of Physics and Department of Physiology and Biophysics
State University of New York
Buffalo, New York 14260

METHODS IN CELL BIOLOGY, VOL. 89

0091-679X/08 $35.00
DOI: 10.1016/S0091-679X(08)00621-3

Abbreviations

FRET	Förster Resonance Energy Transfer
ET	Energy Transfer
FLIM	Fluorescence Lifetime Imaging Microscopy
EYFP	Enhanced Yellow Fluorescent Protein
FP	Fluorescent Protein, such as GFP (green), CFP (cyan), YFP (yellow), RFP (red), and others
TCSPC	Time-Correlated Single Photon Counting

Abstract

The understanding of cell function often requires that complex intracellular pathways are considered in quantitative terms. The access to precise measurement of activities in live cells is increasingly provided by the advances in fluorescence lifetime imaging microscopy (FLIM) of Förster (or fluorescence) resonance energy transfer (FRET)-based molecular biosensors. We discuss how quantitative *in vivo* imaging can be combined with *in vitro* biochemical characterization to develop computational systems models simulating the behavior of biochemical networks. We describe the application of such approach in computational modeling of the Ran GTPase function in mitotic spindle assembly. The RanGTP concentration gradient surrounding mitotic chromosomes induces the formation of a gradient of spindle assembly factors (SAFs) activated by RanGTP-induced release from inhibitory complexes of SAFs with importin β. To visualize the gradient of activated SAFs in live cells, we used FLIM to detect the signal of a FRET-based biosensor that reports its RanGTP-induced liberation from importin β. We review the technical aspects of FRET measurements by FLIM and discuss the step-wise design of systems models aided by quantitative imaging. As evidenced by the

example of mitotic Ran gradient studies, the computational simulations are a powerful tool to test new hypotheses on biological function.

I. Quantitative Imaging and Systems Modeling as a Tool in Cell Biology—The Rationale and Strategy

To understand a cell's response to a stimulus or perturbation, it is often insufficient to rely on qualitative picture of the regulatory networks involved in the response. The requirement to consider the biochemical interactions in live cells quantitatively is being met by advances in quantitative *in vivo* imaging with molecular biosensors. Combined with the accumulated knowledge acquired by more traditional *in vitro* biochemical techniques, many fields in cell biology now have access to large amount of data describing the behavior of biological networks. However, the complexity and dynamic nature which is characteristic of biological systems make the analysis of such data challenging and have spurred a development of novel methods, sometimes collectively referred to as *computational systems biology* (Kitano, 2002).

Computational systems biology offers two types of general approaches: identification of patterns from the often vast amounts of experimental data and a hypothesis-driven approach relying on the simulation of the biological systems behavior in mathematical models (Kitano, 2002). In particular, the latter parsimonious approach is appealing to cell biologists because it rigorously tests current hypotheses and does not require complete quantitative description of all biological system components. Instead, a minimal sufficient description of the biological process in question is used to develop the mathematical model for simulations, typically relying on already published data. However, the combination of both strategies is optimal and can be achieved in a step-wise process of simulation and implementation of new experimental data into the model.

In Fig. 1, we illustrate how the computational models based on biochemical *in vitro* measurements can be combined with quantitative *in vivo* imaging data to refine the computational model for simulations.

1. A computational model is built representing the biological system at equilibrium state (Alves *et al.*, 2006). The model includes a minimal defining set of biological system components, their regulatory connections, their concentrations, and kinetic parameters of their reactions obtained from published literature or measured (Fig. 1A). The parameters of not yet characterized system components are adjusted to produce a model matching the known parameters at equilibrium.

2. A molecular sensor is constructed to quantitatively report on the behavior of one of the components in the experimental system. For measurements in live cells, it is practical to design a sensor as a genetically encoded fluorescent protein (FP)-tagged Förster Resonance Energy Transfer (FRET) pair, either as two interacting proteins or a single Cameleon-like (Mitra *et al.*, 1996; Miyawaki *et al.*, 1999; Tsien *et al.*, 1993) molecule. The specificity of the sensor is evaluated in *in vitro*

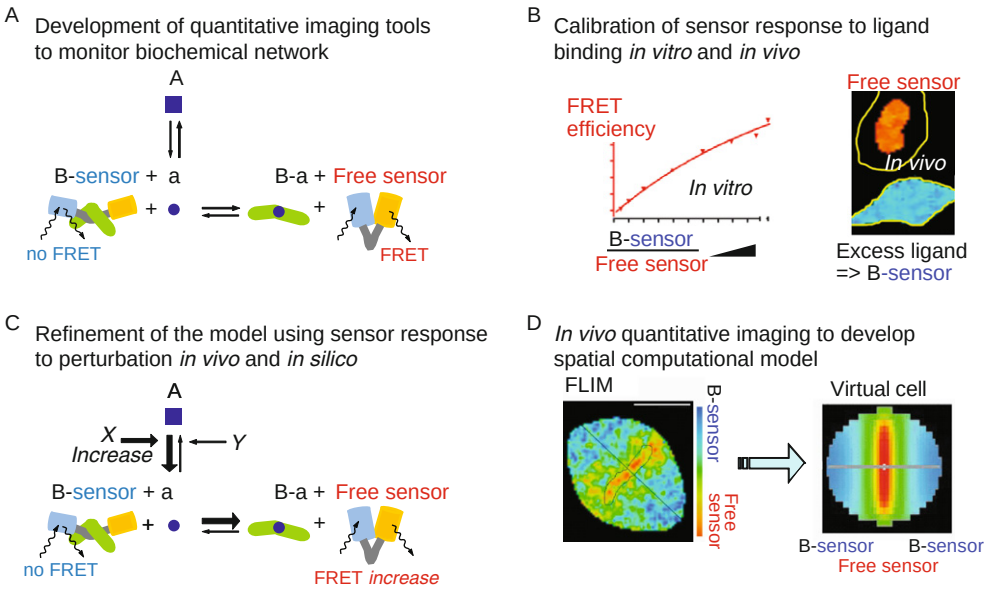

Fig. 1 Schematic diagram describing step-wise development of a computational Ran systems model guided by the application of a quantitative Förster (or fluorescence) resonance energy transfer (FRET) biosensor. A computational model was designed consisting of a minimal sufficient set of reactions controlling the guanine nucleotide exchange and GTP hydrolysis on Ran and the coupling of RanGTP production to the RanGTP-regulated binding of NTRs to their cargos. In the model, available published kinetic parameters and reactant concentrations were used and unknown parameters were fitted to obtain a model approximating the known behavior of the Ran system at equilibrium. (A) A FRET-based biosensor was developed to monitor the dynamics of RanGTP-regulated importin β cargo release quantitatively and in a nondestructive fashion in a variety of *in vitro* as well as *in vivo* conditions. In the diagram shown, "a" corresponds to RanGTP, A = RanGDP, B = Importin β, and the sensor is Rango. Provided that a FRET-based sensor mimicking the behavior of a system's component can be created, a similar approach is applicable in the design of computational models of other intracellular pathways. (B) The signal of the sensor (Rango) was calibrated *in vitro* by measuring the changes of its FRET efficiency to increasing concentrations of its ligand, recombinant purified importin β. Assuming the measured apparent dissociation constant of the Rango–importin β interaction ($K_d = 2$ nM), the fractional occupancy of Rango across the range of importin β concentrations was calculated and a dose–response calibration curve was fitted to the measurements. (C) To quantify the RanGTP-induced release of importin β cargos in the cytoplasm, increasing concentrations of GTP hydrolysis-deficient Ran mutant (RanQ69L) protein were added to functional mitotic *Xenopus laevis* egg extracts containing Rango. The corresponding increase of importin β dissociation was signaled by increase of Rango FRET. Conversely, the addition of importin β to the extracts increased the fraction of importin β-bound cargos, decreasing Rango FRET. The changes of free Rango fraction were calculated from FRET measurements in the cytoplasmic extracts, assuming the dose–response calibration curve obtained with purified proteins (above, C). In turn, such measured perturbation-induced changes of the cytoplasmic free Rango fraction were used as a guide to further refine the fitted parameters of the minimal computational Ran systems model. (D) Quantitative spatial imaging of the mitotic RanGTP-regulated gradient of importin β cargos in live cells guide the development of spatially resolved computational Ran systems models.

experiments with purified components. Next, the biochemically verified sensor–ligand binding is correlated with measurements of sensor's FRET signal by a variety of methods, including fluorescence lifetime imaging microscopy (FLIM). *In vitro* measurements with purified sensor and its ligand are used to determine the apparent dissociation constant of the sensor–ligand interaction (K_d). Also with purified proteins, the response of the sensor donor lifetime τ_{DA} to increasing concentration of the ligand is measured by FLIM. Assuming the measured K_d, a dose–response curve is then calculated that expresses how τ_{DA} changes depending on the proportion of the sensor molecules bound to the ligand (FRET efficiency/fractional occupancy calibration curve, Fig. 1B, left). Given the robustness of the FRET measurements by FLIM, such *in vitro* calibrations can be used to estimate the fractional occupancy of the sensor in live cells imaged by FLIM microscopy.

In case of a FRET sensor responding to its posttranslational modification rather than ligand binding, the calibration curve could be obtained by measuring samples containing known mixed proportions of fully modified and unmodified sensor. If the *in vitro* calibration is unavailable for technical reasons, the extreme physiological readings of the sensor may be obtained *in vivo* (in cells or extract) by treatments presumably fully activating or inhibiting the sensor (Fig. 1B, right).

3. The sensor is introduced into the otherwise unperturbed biological system (corresponding to the equilibrium state of the computational model) and its FRET signal is measured by FLIM. For example, the sensor is expressed in cells or added to the *Xenopus laevis* egg extracts. The dose–response data obtained *in vitro* (point 2 above) are then used to calculate the fractional occupancy of the sensor with its ligand in such *in vivo* system existing at its "equilibrium" state. Such estimates are then used to adjust the fitted parameters of the computed model simulating the presence of the sensor in the system. For example, the unknown concentrations of endogenous sensor ligands are changed in the model to match its measured fractional occupancy *in vivo*. Next, the signal of the sensor is measured by FLIM in response to experimental perturbations of the biological system. For example, live cells or functional extracts containing the sensor are treated with inhibitors or activators of the pathway in question, or with increasing concentrations of the ligand. The change of the fractional occupancy of the sensor measured by FLIM is then used to further refine the computed model (Fig. 1C).

4. The refined nondimensional computational model can be used to analyze quantitative imaging data obtained in cells. The combination of nondimensional modeling and cell imaging is then used to guide the construction of spatially resolved computational systems models. Such models encompassing the combined knowledge on the intracellular network provide rigorous tests of current hypotheses. In addition, these lead to otherwise unavailable insights into cellular function and aid the formulation of new functional hypotheses. Importantly, the computational systems models can be easily shared between different laboratories and evolved by implementing new data measured in live cells (Fig. 1D).

II. Quantitative Detection of Biochemical Interactions by FLIM

A. Introduction to FRET and FLIM

FRET is nonradiative transfer of energy from an excited donor fluorophore (D) to an acceptor (A). The efficiency of energy transfer (E) is inversely proportional to the sixth power of the distance between the fluorophores R (Förster, 1946, 1948):

$$E = \frac{R_0^6}{R_0^6 + R^6}$$

The Förster distance R_0 at which E is 50% is specific for each fluorophore pair. R_0 depends on the spectral overlap of donor and acceptor J, the orientation factor κ which is a function of the angles between the chromophore dipoles, the quantum yield of the donor Q_d, and the refractive index n of the medium (Clegg, 1966; Förster, 1946, 1948):

$$R_0 = 9.78 \times 10^3 \left(Q_d \kappa^2 n^{-4} J\right)^{1/6} \mathring{A}$$

E is commonly measured by exciting the donor and determining the intensity of the peak emissions from both fluorophores. The estimate of FRET efficiency is often calculated as the ratio of the intensity emitted at the acceptor wavelength to the total intensity emitted. However, E can also be directly derived from the measurements of the fluorescence lifetime of the donor τ_D (Gordon *et al.*, 1998), which is the principle of FLIM.

After absorbing the energy from a photon, the fluorophore remains in an excited state until it returns to the ground state by emitting a photon, releasing the energy difference in the form of heat or transferring the energy to another nearby molecule. Since the relaxation to the ground state is stochastic, the lifetimes of fluorophore molecules in the excited state are exponentially distributed (Lakowicz, 1999). The characteristic fluorescence lifetime τ of a fluorophore is the time after which e^{-1} molecules of the original populations remain in the excited state. If the excited fluorophore is located near a molecule that can accept its emission energy, the additional decay path out of the excited state shortens the lifetime. The FRET efficiency then corresponds to

$$E = 1 - \frac{\tau_{DA}}{\tau_D},$$

where τ_{DA} is the donor lifetime in the presence of acceptor and τ_D in its absence (Tsien, 2003). Because the fluorescence lifetime is an intrinsic molecular property of the fluorophore, it is independent of the fluorophore concentration and can be compared between instruments, laboratories, and samples. In practice, the τ_D can be considered as a constant (corresponding to, e.g., the lifetime of the recombinant donor molecule measured *in vitro* or an arbitrary number), and the only variable needed to be measured in live cell imaging with FLIM is the τ_{DA}. The advantage of FLIM is that the measurements of τ_{DA} are in principle not influenced by

concentration of the fluorophores, by the effects of donor on acceptor fluorescence, and by direct excitation of the acceptor, that is, the typical problems greatly complicating FRET detection by other methods. The presently available instrumentation, fluorophores, and analysis software make it possible that within a wide range of conditions typical for many cell biological samples, the detection of FRET by FLIM can deliver its promise also in experimental practice.

B. Other Modes of FRET Microscopy as Controls for FLIM

For the successful application of FLIM, it is important to realize that the detection of FRET in biological samples by any technique is influenced by many variables. These variables include the biochemical and photophysical properties of the FRET sensor, the spectral properties of the sample, the detection instrument, and the physics of the process used for the detection. Any of these factors can contribute to detection artifacts and erroneous conclusions. Although FLIM has distinct advantages over other FRET detection methods, it is by no means an exception to the requirement for rigorous controls. Arguably the most straightforward approach is to seek consistency of results across independent FRET detection methods to validate FLIM results. Likely, one or more such methods would be available in many FLIM-capable laboratories and should be combined with biochemical controls to verify the interactions of the biosensor presumably detected by FLIM. In the study of the RanGTP gradient in somatic cells, we combined spectral analysis of the Rango sensor in a spectrofluorimeter, epifluorescence intensity ratio imaging, donor fluorescence intensity change after acceptor bleach, and time-correlated FLIM with extensive biochemical characterization of the sensor (Kalab *et al.*, 2006).

Most epifluorescence microscopes can be adapted for the detection of FRET by wide-field *epifluorescence intensity ratios*. Typically either the increased emission of the donor and decreased emission of the acceptor are used (Erickson *et al.*, 2001), and normalized to the amount of protein by measuring the directly excited acceptor emission as well (Kalab *et al.*, 2002, 2006). The contemporary highly sensitive and fast CCD cameras can provide excellent speed of acquisition and sufficient resolution. However, out-of-focus artifacts typical to wide-field acquisition may greatly complicate FRET detection in structures with small vertical dimension. Any intensity ratio technique requires extreme care to account for varying background and autofluorescence in the samples, spectral overlaps between the donor and the acceptor, and for example, for flickering of Mercury lamps used for excitation. Although quantitative FRET measurement based on intensity ratios is challenging, it is potentially an excellent qualitative control to validate FLIM results.

The measurements of *donor fluorescence intensity change after acceptor bleach* performed with a laser scanning confocal microscope is a relatively robust and straightforward method of semi-quantitative FRET detection in cells. One of the disadvantages of the ''acceptor bleach'' method is that the motion of the imaged cell and structures within it during the bleaching period often causes shifts between

pre- and post-bleach images that cannot always be remedied by postimaging realignment. Temporal changes also cannot be measured because it is a photodestructive method. The optimal bleaching of YFP without bleaching CFP would require a 540-nm laser but the 514 nm line of the Argon laser is often the closest available. The optimal excitation wavelength for CFP (around 435 nm) is not provided by the spectrum of Argon/Krypton laser, whose closest line of 458 nm produces strong direct excitation of YFP. Thus, high-quality, CFP-selective emission filters are essential. Despite such drawbacks, in the study of the mitotic Ran gradient in HeLa, we found an excellent correlation between the relative E estimated by acceptor bleach method and FLIM results obtained in cells imaged under a variety of experimental treatments (Kalab *et al.*, 2006; and data not shown).

C. Design of FRET-Based Sensors for FLIM Applications

In addition to the currently prevalent use of FPs as a donor and acceptor, organic fluorescent molecules linked to proteins offer several potential advantages, such as better spectral properties, smaller size, and lower environmental sensitivity (Alves *et al.*, 2006). In some cases, functional donor and acceptor molecules can be created by relatively nonspecific covalent *in vitro* modification of recombinant proteins by commercially available dyes (Caudron *et al.*, 2005). There is also promising progress in specifically targeted labeling of proteins, for example, via a tag that is subsequently modified by small organic fluorescent molecule (Johnsson and Johnsson, 2007), and in the use of nonnatural fluorescent amino acids to produce a FRET sensor (Kajihara *et al.*, 2006).

However, at present, the FRET sensor design based on FPs is a more mature technology readily applicable for many *in vivo* applications and FLIM measurements. Genetically encoded FP-based FRET biosensors may be formed by two molecules labeled by donor and acceptor fluorophore. The interaction of the two labeled molecules will be detected by increased FRET between the donor and acceptor. In particular, if the concentration of the donor and acceptor can be accurately controlled, the bimolecular sensor design is well suitable for quantitative FLIM (Caudron *et al.*, 2005). Compared to intensity-based FRET detection methods, FLIM is an advantageous approach if the donor and acceptor concentrations locally vary within cells because the τ_{DA} measurement is insensitive to FP concentration. However, if the donor and acceptor concentrations are highly disproportionate, it is critical to ensure tight separation of the donor fluorescence emission by good choice of the FP pair and by the use of stringent emission filters.

In comparison, in the single-molecule FRET biosensor, the donor and acceptor molecules are present at equimolar concentrations throughout the cell, simplifying the FLIM acquisition and analysis. Such a sensor is constructed as a peptide chain containing a sensory domain flanked by donor and acceptor FPs at its N- and C-termini, respectively. The binding of a ligand induces a conformational change of the sensor peptide and a concomitant change in the distance and orientation of the FPs at its termini (Fig. 2). The resulting change of FRET between the FPs

provides readout of ligand binding to the sensor domain. Such a design principle was pioneered by the calmodulin domain-based calcium indicator Cameleon (Mitra *et al.*, 1996; Miyawaki *et al.*, 1999; Tsien *et al.*, 1993) and was subsequently applied to the design of FRET probes that detect many different ligands. While Cameleon closes upon calcium binding (Mitra *et al.*, 1996; Tsien *et al.*, 1993), ligand-induced extension of the sensory domain is equally effective (Kalab *et al.*, 2002) (Fig. 2). Cameleon-like sensors can also detect posttranslational sensor modifications such as induced by phosphorylation (Niethammer *et al.*, 2004).

Successful design of a Cameleon-like FRET probe requires that its sensory domain undergoes significant reversible conformational changes. Because of the size of GFP-derived FPs, the minimal separation of their fluorophores is ~3 nm. The distance at which the FRET is barely detectable corresponds usually to $1.5 \times R_0$, that is, 7–8 nm for the FPs (Lakowicz, 1999). Because E decreases with

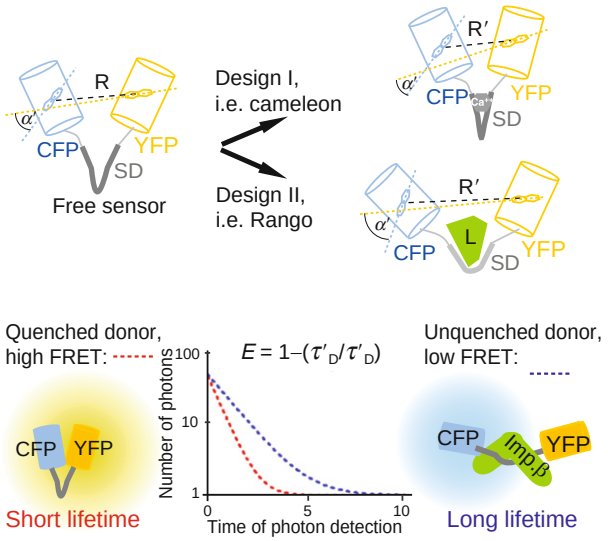

Fig. 2 (Top) Commonly used single-molecule Förster (or fluorescence) resonance energy transfer (FRET) sensors consist of donor–acceptor fluorescent protein (FP) pair (e.g., cyan FP as a donor and yellow FP as an acceptor) linked by a sensory domain (SD). The specific binding of a ligand to SD induces conformational change of the SD, inducing change of the distance (R) between the donor and acceptor FPs and/or of their fluorophore orientation (α–α'). As a result, the FRET efficiency changes upon ligand binding to the SD. In the Ca^{++} sensor Cameleon, the donor and acceptor become closer upon Ca^{++} binding to its SD (calmodulin), increasing FRET, while the binding of importin β to the SD in Rango [where the SD is importin β binding (IBB) domain of importin α] pushes the FPs apart, quenching FRET. (Bottom) In free Rango (left), FRET occurs with high efficiency E due to short distance between the donor and acceptor FPs, compared to Rango bound to importin β (right). The increased FRET efficiency in free Rango results in lower emission intensity from the donor FP, corresponding to the donor FP's shorter fluorescent lifetime τ'_D

the sixth power of the distance, increasing the amplitude of the donor–acceptor distance in the open versus closed conformation has lesser influence on improving the performance of the sensor, as compared to the effect of shortening the average distance between FPs. The minimal distance of FPs in the closed sensor conformation should not exceed the R_0 (~5 nm for many current FPs).

Often, published structural data can guide the FRET sensor design (Kalab *et al.*, 2002). The distance between FPs separated by an unstructured peptide can also be estimated based on its sequence and the model of a worm-like chain (Bustamante *et al.*, 1994; Ohashi *et al.*, 2007). The first choice after identification of a suitable sensory domain is to trim to a minimal functional domain. However, as the FPs may affect the sensor domain mobility and the access of its ligand (in particular if the ligand is a macromolecule), this should be considered carefully. It is a good precaution to create the connections of the sensory domain with FPs as short flexible peptides (such as GGSGGS; Evers *et al.*, 2006) to allow free mobility of the FPs. If the sensory domain is rigid and relatively large in the closed conformation, the addition of longer flexible linkers may increase FRET as the FPs may be allowed to move closer to each other. The distance between FPs in a FRET probe can be shortened by removing up to 5 N-terminal and 11 C-terminal amino acids from the FPs without loss of fluorescence (Shimozono *et al.*, 2006). To minimize potential nonspecific interactions, the open reading frame of the FRET probe should be kept as small as possible and devoid of unnecessary peptide sequence on its N- and C-terminal termini. Bulky protein tags added to FPs (such as protein A domain, GST) may interfere with the function of the sensory domain and decrease the probe's signal amplitude (P.K., unpublished data). Among smaller epitope tags, one should avoid 6His, which displays mild toxic effects when expressed in tissue culture cells (P.K., unpublished data).

After choosing the sensor design, the biggest gain in FRET probe performance comes from the selection of the donor–acceptor FP pair. In addition to the semirational improvements of genetically encoded fluorophores by point mutagenesis, molecular "breeding" by evolutionary selection performed in the laboratory (Rizzo *et al.*, 2004; Shu *et al.*, 2006; Tsien, 2006; Wang and Tsien, 2006; Zacharias and Tsien, 2006) resulted in a spectacular array of fluorophores available to contemporary cell biology (Giepmans *et al.*, 2006). We will only briefly point to the desirable characteristics of FPs for FLIM.

1. A donor with a *single exponential fluorescence lifetime* is preferred. A single exponential lifetime can be determined to better than 10% precision by counting less than 200 photons (Kollner and Wolfrum, 1992), while a similar precision in measurements of a biexponential lifetime requires at least 10–100 times more photons. Multiple fluorescence decay components are indicative of an undesirable biochemically nonhomogeneous donor protein population. If the donor displays more than one decay component but one is strongly dominant (such as Cerulean (Yasuda *et al.*, 2006), it is possible to approximate the donor lifetime as a single exponential decay (Kalab *et al.*, 2006).

2. The requirement for *large FRET signal changes* of the donor–acceptor pair is balanced with the requirement for dominant single exponential decay pattern of the donor. While the ECFP–EYFP pair displays larger FRET signal changes compared to Cerulean–EYFP as detected by intensity ratio measurements (Nguyen and Daugherty, 2005; P.K., unpublished data), the Cerulean–EYFP pair provides significantly more robust FLIM measurements *in vitro* and in live cells (Kalab *et al.*, 2006) and is therefore preferable.

3. Fast and complete maturation of both FPs, in particular the acceptor, is essential. If rapidly maturing donor molecules would be linked to slowly maturing acceptors, erroneously long fluorescence lifetimes would be recorded (low FRET). An excess of immature nonfluorescent donor molecules would decrease signal and complicate the fluorescence lifetime analysis as well.

4. Good photophysical properties, in particular slow bleaching rate, no blinking, and low sensitivity to local environmental parameters (e.g., pH) are desirable. Although such parameters have been published for some available FPs, controls for such variables should be run in any given experimental system. For example, FLIM measurements of a donor FP expressed by itself in a cell (i.e., without acceptor) should yield homogeneous fluorescence lifetime throughout the nucleus and cytoplasm, thus providing a basic assurance that the donor is not overtly environmentally sensitive.

It is important to consider that excitation of FP chromophores produces reactive oxygen species that can react with other molecules adjacent to FPs and thus potentially influence the behavior of the sensory domain in the FRET probe, the FP donor lifetime, and the physiology of the imaged cells (Remington, 2006). FPs can significantly differ in how much their fluorescence lifetimes are affected by photobleaching. Photobleaching of ECFP strongly shortens its fluorescence lifetime (2.59 vs. 1.59) compared to EGFP which is much less sensitive in that regard (2.64 vs. 2.56 ns) (Tramier *et al.*, 2006).

D. Donor–Acceptor FP Pairs Suitable for FLIM

Some of the most widely used FP pairs for FRET are derivatives of the CFP (a GFP with the mutations Y66W, N146I, M153T) and YFP (a GFP with the mutations S65G, V68L, Q69K, S72A, T203Y) (Tsien, 1998). The chromophore of the ECFP may exist in several conformations resulting in multiple fluorescent states and lifetimes (Rizzo *et al.*, 2004; Yasuda, 2006). An improved, —two to three times brighter ECFP variant called Cerulean was obtained by introducing mutations predicted to stabilize one preferred conformation (H148D) and to improve its maturation (S72A, Y145A) (Rizzo *et al.*, 2004). Cerulean still exhibited detectable two-exponential decay, in contrast with single-exponential decay of GFP and Venus (Tramier *et al.*, 2006; Yasuda *et al.*, 2006; A.P., unpublished data).

Improved donor–acceptor pairs were *in vitro* evolved that strongly outperformed the original CFP–YFP (Nguyen and Daugherty, 2005). The best pair called CyPet–YPet displayed a sevenfold increase in the FRET signal amplitude compared to CFP–YFP (Nguyen and Daugherty, 2005). Also the amplitude of the donor lifetime changes in the CyPet–YPet probe ($\tau_{no\ FRET}$ = 2.43 ns)/($\tau_{max\ FRET}$ = 0.53 ns) was markedly increased compared to CFP–YFP ($\tau_{no\ FRET}$ = 2.99 ns)/($\tau_{max\ FRET}$ = 1.87 ns) (Nguyen and Daugherty, 2005). The increase of ET in CyPet–YPet pair depends on increased intramolecular CyPet to YPet binding induced by the S208F mutation in YPet (Ohashi *et al.*, 2007). In sensors where the donor–acceptor dimerization would compete with high affinity ligand binding, such a relative drawback can be outweighed by significant gain in the signal amplitude.

The photophysical properties of enhanced GFP [mutation S65G] (Tsien, 1998) (single-exponential fluorescence lifetime decay, good photostability, and fast maturation) (Jung *et al.*, 2005; Yasuda *et al.*, 2006) make it one of the best available donor FPs. Excellent performance of EGFP as a donor in FLIM measurements was observed with various coral-derived red FPs as acceptors (Peter *et al.*, 2005; Yasuda *et al.*, 2006). The major limitation of the currently available RFPs as acceptors for EGFP remains relatively slow and/or incomplete maturation, estimated to represent 40–50% (Yasuda *et al.*, 2006) and the tendency of some to aggregate.

Attempts were made to generate ''dark'' acceptors, that is, fluorophores that are good acceptors of FRET but emit the transferred energy by thermal loss with minimal fluorescence. REACh (Resonance Energy-Accepting Chromo-protein) is a nonfluorescent YFP mutant (Ganesan *et al.*, 2006) with excellent spectral overlap with EGFP. As REACh is virtually nonfluorescent, in principle no spectral filtering is needed and photons can be collected in the entire spectral window of GFP emission increasing the detection sensitivity. Moreover, the elimination of acceptor fluorescence emission reduces the spectral bandwidth needed by the FRET sensor, and hence is a promising strategy for designing FRET pairs that can be used for simultaneous quantitative FLIM-based detection of multiple protein activities in single cells.

III. Technical Considerations for FLIM in Live Cells

The reported fluorescence lifetime τ_D of FPs ranges between 1 and 5 ns (Nguyen and Daugherty, 2005; Rizzo *et al.*, 2004; Yasuda *et al.*, 2006). However, in FRET-based sensors introduced to live cells, the entire physiologically relevant amplitude of the lifetime may only be a few hundred picoseconds (Kalab *et al.*, 2006). To detect spatially well-resolved intermediate fluorescence lifetime values in cells, the fluorescence lifetime therefore often needs to be measured with the precision of few tens of picoseconds.

A. Time- and Frequency-Domain FLIM

Two alternative approaches to fluorescence lifetime measurements are currently used: (1) in time-domain FLIM, a very short laser pulse excites the fluorophores in the sample and the time until the arrival of a fluorescent photon to a time-correlated detector is measured; or (2) in frequency-domain FLIM, the intensity of the excitation light is modulated and the detected lag of the fluorescence emission phase and decrease of its amplitude is used to calculate the donor lifetime (van Munster and Gadella, 2005) (Fig. 3). In both approaches, pixel-by-pixel fluorescence lifetime 2D ''image'' of the sample is calculated and displayed.

A variety of light sources such as LEDs, lasers, and lamps can be used for the donor fluorophore excitation in frequency-domain FLIM as long as the excitation light can be modulated. A reliable resolution of multiexponential decays requires that a wide range of excitation frequencies is used (van Munster and Gadella, 2005). However, the typically available fractionally modulated sinusoidal excitation extracts lifetime information out of only a small fraction of the photons (Philip and Carlsson, 2003). Hence, frequency-domain FLIM in practice requires relatively bright samples. On the other hand, the frequency-based FLIM can be significantly faster than time-domain measurements because the fluorescence emission can be recorded at all pixels simultaneously as in wide-field fluorescence microscopy. The commercially available instrumentation for frequency-domain FLIM (Lambert Instruments; http://www.lambert-instruments.com/, Jobin Yvon Horiba; http://www.jyinc.com/) can be installed on most epifluorescence microscopes and are significantly less expensive compared to typical time-domain FLIM setups.

In the most commonly used version of time-domain FLIM measurement, *t*ime-*c*orrelated *s*ingle *p*hoton *c*ounting (TCSPC), the sample is excited with a very short light pulse, and the arrival time of the first fluorescent photon to the detector is measured (Becker *et al.*, 2004; Suhling *et al.*, 2005). After registering the first photon, the detector is blind to following photons for a characteristic time period, the dead-time. Because only the first photon is registered, the excitation intensity, detector sensitivity, and detection time window must be matched so that at most one photon arrives to the detector during one detection time window. Otherwise, the measured photon distribution would be biased toward shorter lifetimes. Such measurement scheme works best for relatively weakly fluorescent samples with short lifetimes such as FPs. Time-domain FLIM builds an intensity versus time decay curve directly during the measurement. Visual inspection of this decay curve allows immediate judgment of the data quality and fitting of even complex multiexponential fluorescence lifetime decays is straightforward. Commercial providers of TCSPC FLIM equipment include Becker & Hickl (http://www.becker-hickl.de/), PicoQuant (http://www.picoquant.com), and Horiba Jobin Yvon (http://www.jyinc.com).

The nanosecond lifetime of FPs requires a pulsed excitation source with picosecond and shorter pulses. The mode-locked Ti:Sapphire laser system providing 150fs infra-red (IR) pulses are used to excite the FPs via two-photon (2p)

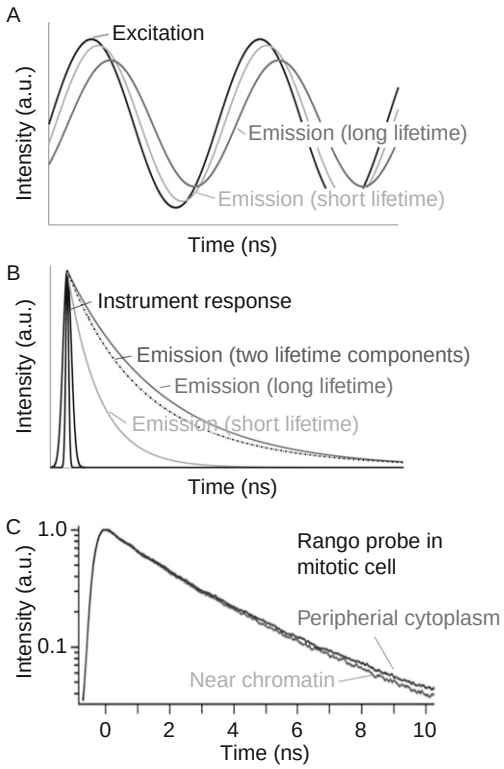

Fig. 3 Principles of (A) frequency-domain (FD) (B) and time-domain (TD) fluorescence lifetime imaging microscopy (FLIM): (A) In FD-FLIM, the sample is excited using light with modulated intensity. A larger phase lag of the fluorescence emission behind the intensity-modulated excitation indicates a longer lifetime. (B) In TD-FLIM, the sample is excited using a pulsed light source and the exponential decay of the fluorescence intensity is measured directly. A longer single exponential decay is easily distinguished from a short lifetime. With sufficient data, even small changes in lifetimes are measurable, and double exponential decays can be determined correctly. (C) Current FLIM instrumentation can measure and spatially resolve small differences in fluorescence lifetime of Förster (or fluorescence) resonance energy transfer (FRET) biosensors expressed in live cells. Shown is an example of Rango fluorescence lifetime decay profiles measured in a live mitotic HeLa cell near chromatin and at the periphery of the same cell.

absorption (Denk and Svoboda, 1997; Denk *et al.*, 1990; Helmchen and Denk, 2002). Alternatively, frequency doubling of the IR pulse may be used to create short pulses of visible light covering a wide range of excitation maxima typical for FPs. Compared to the 2p excitation, the available wider confocal sections in frequency doubled excitation are advantageous in samples containing low concentration of homogeneously distributed donor (Kalab *et al.*, 2006). Pulsed laser diodes offer an economical alternative excitation source to expensive Ti:Sapphire laser systems. However, the pulse duration of the diode lasers is significantly longer and output power dependent, averaging 40–50 ps per pulse at minimal power, increasing

to 100 ps with increased power. This pulse length may challenge the detection of small changes in fluorescence lifetime. In the future, broadband continuum lasers might provide a good pulsed excitation source for TCSPC (Owen *et al.*, 2007). For costs between a Ti:Sapphire laser system and single diode lasers, these lasers provide 2 ps pulses over the entire useful excitation spectrum.

B. The Limitations of TCSPC FLIM

TCSPC FLIM dataset is sequentially composed by scanning from pixel-to-pixel. The galvanometer-driven scan heads in commonly available confocal scanning microscopes provide enough accuracy and speed to match the detection capacity of high quality TCSPC FLIM equipment. At each pixel, individual photons are counted to build up the fluorescence lifetime decay curve. The scanning rate and the rate at which the photons are counted per pixel determine the time needed to acquire one complete FLIM dataset.

The need to determine precisely the time between the excitation pulse and the detection for each detected photon requires processing the photons one-by-one. The rate at which individual photons can be detected and counted is called count-rate and represents the bottle neck for speed for TCSPC FLIM. The maximal count-rate is limited by the instrumentation used and the sample:

1. A Ti:Sapphire laser provides excitation pulses with ~80 MHz repetition rate.
2. GFP's have fluorescent lifetimes between 2 and 5 ns which means that the tail of the fluorescent decays reaches past the 12.5 ns interval of the Ti:Sapphire pulses.
3. The detection electronics consisting of detector and counter may process photons at rates between 1 and 10 MHz depending on the model [according to datasheets from Becker & Hickl (http://www.becker-hickl.de/) and PicoQuant (http://www.picoquant.com/)].

The maximal rates possible with particular detection electronics therefore appear to limit the maximal count rate for TCSPC FLIM. However, absorption and emission of photons are stochastic processes so that it is impossible to generate always exactly one fluorescent photon to hit the detector at the maximal count rate. As the rate of emitted photons reaches the detection speed, it becomes likely that two photons arrive within the same detection interval. This would lead to an error in the lifetime estimate as only the first of the two would be counted. Hence, typical useful counting rates in TCSPC FLIM are an order of magnitude lower than the maximal detection rates.

For example, at a 500-kHz count rate, the 200 photons per pixel that are sufficient to determine a single exponential decay to better than 10% precision (Kollner and Wolfrum, 1992) under ideal conditions could be counted in 0.4 ms. However, *in vivo* measurements with a background typical for biological samples often require 10 times more counts (Philip and Carlsson, 2003). Hence acquiring an *in vivo* image of 128 × 128 pixels would require about 1min at 500 kHz count rate

and theoretically, a proportionally shorter time with faster TCSPC FLIM boards. As the counting capacity of the contemporary FLIM equipment increases, the number of FRET donor molecules that can be expressed and excited in the sample without perturbing the biological system is becoming a limiting factor.

C. The Use of Tissue Culture Cells for Quantitative FRET Detection by FLIM

The precise measurement of the donor fluorescence lifetime for quantitative FLIM FRET requires optimization of the signal to noise ratio in the spectral window of the donor emission. Unfortunately, the emission of the CFP-related donors overlaps with major sources of autofluorescence in cells such as flavins, NADH, and lipids (Monici, 2005). The very short fluorescence lifetime of NADH (emission peak 450–460 nm, $t = 0.4$ ns) (Lakowicz *et al.*, 1992) and flavins ($\sim$0.3 ns; Chorvat and Chorvatova, 2006) can in principle be separated from the CFP lifetime. Other autofluorescence sources, such as protein-bound NADH (emission 435 nm, $t = \sim$2 ns; Lakowicz *et al.*, 1992; Skala *et al.*, 2007) may be suppressed by using narrow emission filters. However, conditions that negatively influence cell vitality (confluence, ageing, oxidative stress, apoptosis, necrosis) typically induce strong autofluorescence that can change over a wide spectrum of emission wavelengths and fluorescence lifetimes. The autofluorescence detected in MCF10A breast cancer cells in tissue culture showed complex multiexponential pattern whose components and their proportions changed depending on the plating density (Bird *et al.*, 2005). While filtering out the background autofluorescence, either through its characteristic lifetime or spectrally may be possible in postacquisition analysis, completely relying on such approach is therefore not advisable.

In order to obtain reproducible and indeed meaningful FLIM measurements, the best practice is to limit the analysis to cell samples that are in a reproducible physiological state. In case of tissue culture cells, this would typically mean to only perform experiments analyzed by FLIM in healthy, nonconfluent cells that do not display strong autofluorescence.

The commonly used tissue cell cultures are composed of phenotypically diverse collection of cells differing in size, shape, growth rate, adherence, vitality, and so on. If individual cells are propagated in isolation, it is readily observable that such phenotypic differences can be maintained over a number of cell division. On the other hand, any change in culture conditions (stress, overgrowth, change of media type) can lead to significant selection drift and change of the cell sample used for analysis. In our experience, the effect of the cell-to-cell variation on quantitative analysis of intracellular pathways by FRET-based methods can be significantly suppressed by working with single cell-derived ''monoclonal'' cell cultures. At the same time, such an approach allows one to better evaluate the physiological significance of the variability detected between cells.

We recommend the following steps to maximize the reproducibility of FLIM/FRET detection in tissue culture cells:

1. Start with a verified cell stock from a reputable source, such as ATCC. Do not use any poorly documented cells or cells held for many passages in culture. Regularly inspect and test the cells for the presence of infection such as mycoplasma.

2. Establish a robust protocol that will reproducibly deliver cells in optimal health and confluency for the days of the FLIM experiment.

3. The cell-to-cell variability of the recorded data may represent phenotypic variability between cells in culture. The existence of such variability can be evaluated and controlled for in experiments with "monoclonal" cell cultures (see Section V).

IV. Analysis of the Mitotic RanGTP Gradient Function by FLIM and Computational Modeling

A. Ran-Nuclear Transport Receptor System

Ran is a conserved small nuclear GTPase related to Ras. The Ran-specific guanine nucleotide exchange factor RCC1 binds chromatin and is imported to the nucleus, while Ran GTPase activating protein RanGAP is cytoplasmic throughout the cell cycle. Because both RCC1 and RanGAP catalyze $\sim 10^5$-fold increase in the respective intrinsic activities of Ran, the nucleotide charge of Ran is dominantly influenced by the local concentration of both regulators. As a result, more RanGTP exists around chromosomes and more RanGTP is converted to RanGDP at the periphery of the cell, giving rise to a RanGTP gradient which marks the position of the chromatin throughout the cell cycle (Hetzer *et al.*, 2002).

The RanGTP gradient provides directionality to nucleocytoplasmic transport across nuclear envelope in interphase cells by regulating interactions between nuclear transport receptors (NTRs) of the importin β family and their cargos (Pemberton and Paschal, 2005; Weis, 2003). RanGTP concentrated in the nucleus dissociates complexes of importins with nuclear localization signal (NLS) containing cargos, resulting in nuclear accumulation of cargos. On the other hand, nuclear export receptors (exportins) bind stably to nuclear export signal (NES) containing cargos only in the presence of RanGTP. The heterotrimeric RanGTP–exportin–NES cargo complexes transit through nuclear pore complexes to the cytoplasm where their disassembly is induced by RanGAP-catalyzed hydrolysis of GTP on Ran.

The dynamic RanGTP-regulated NTR–cargo assembly/disassembly continues after nuclear envelope breakdown in vertebrate cells undergoing open mitosis, resulting in the formation of diffusion-limited intracellular gradients of RanGTP-regulated importin α/β-free cargos. Importantly, some importin α/β cargos are essential spindle assembly factors (SAFs) and their mitotic function is activated by RanGTP-induced release from the inhibitory complexes with importin α/β (Gruss and Vernos, 2004; Weis, 2003). As a result, the Ran-regulated gradients of liberated

importin α/β cargos are thought to correspond to gradients of activated SAFs that ensure the correct assembly and function of the mitotic spindle in the segregation of the genome to daughter cells (Bastiaens *et al.*, 2006; Weis, 2003).

B. Rango Sensor Design

To visualize the mitotic RanGTP and importin α/β-regulated cargo gradient in living cells, we developed a fluorescence resonance energy transfer (FRET) biosensor termed Rango (*Ran*-regulated importin β car*go*) (Fig. 2) (Kalab *et al.*, 2002, 2006).

Importin β binds to its NLS cargos either directly or via adaptor proteins such as importins α. The importin α/β cargos bind through their NLS to the C-terminus of importin α, where they compete with the very flexible N-terminal importin β binding domain (IBB) of importin α for access. Only when the IBB binds to importin β molecule, inserting deeply into its structure (Cingolani *et al.*, 1999), the NLS cargo can efficiently load on importin α. The high affinity RanGTP binding to importin β displaces the IBB and thus induces rapid disassembly of the importin α/β complex and consequently the IBB-promoted release of the NLS cargo from importin α.

The IBB is unstructured on its own and assumes an extended rod-like conformation in complex with importin β (Cingolani *et al.*, 1999). We exploited this large conformational change to design a sensor detecting the RanGTP-regulated importin α/β-cargo dissociation. The original version of this sensor, called YIC (YFP–IBB–CFP) is composed of IBB from human importin α_1 flanked by EYFP and ECFP at its N- and C-termini, respectively (Kalab *et al.*, 2002). In its free form (i.e., also in the presence of importin β and RanGTP), YIC emits strong FRET signal which is significantly quenched upon importin β binding. The interactions of YIC and importin β were shown to be highly specific (Kalab *et al.*, 2002), allowing the use of the sensor to detect RanGTP-regulated mitotic gradient of liberated importin β cargos around mitotic chromatin in live *Xenopus* egg extracts (Kalab *et al.*, 2002). To detect importin β cargo liberation by FLIM in live cells, we replaced ECFP with Cerulean, and used IBB from Snurportin 1 instead of importin α1, calling this FLIM-optimized sensor Rango. While the results obtained with the original YIC and Rango in cells were similar, Rango was better tolerated by transfected and microinjected mitotic cells. The use of Cerulean in Rango produced more robust and better spatially resolved FLIM detection compared to ECFP-based sensors (Kalab *et al.*, 2006; A.P.,P.K., unpublished data).

C. *In Vitro* and *In Vivo* Calibration of Rango

To quantify the *in vivo* measurement, the FLIM FRET response of the probe needs to be calibrated. Usually this requires that recombinant FRET sensor and its ligand are expressed and purified and then used to obtain full binding curve where the FRET signal of the sensor is used as a readout for the binding (Fig. 1B, left). Such *in vitro* titrations should be done in conditions similar to the *in vivo* FLIM

detection, namely the same temperature, similar pH, and viscosity. However, as it is essentially impossible to exactly mimic *in vitro* complex intracellular conditions, reference FRET data from cells are needed to see whether and how much the behavior of the sensor differs in comparison of the *in vitro* calibration and cell imaging. To obtain reference points, we microinjected HeLa cells with the Rango sensor together with dominant negative proteins expected to cause either full release (nonhydrolyzing RanGTP mutant) or full binding of Rango to importin β (RanGTP binding-deficient importin β mutant) (Fig. 1B, right).

D. Nondimensional Ran System Model

Several research groups are developing software packages to model spatially resolved reaction-diffusion networks and provide the software free to the academic community. The solutions vary in user interface, their way of handling space, and diffusion, and whether they deal with the molecules stochastically or as concentration (Alves *et al.*, 2006). We chose Virtual Cell (Slepchenko *et al.*, 2003) (http://www.nrcam.uchc.edu/) to construct a computation model simulating the GTP/GDP cycle on Ran coupled to a minimal set of NTRs and their cargos. The initial phases of model construction and testing were performed with Jarnac and a set of conditions used for simulation of Ran-regulated nuclear transport (Smith *et al.*, 2002).

Any model of a particular biological reaction network will represent only a subset of the entire network of intracellular reactions. Because of the redundancy and complexity of biological systems, several models might be possible corresponding to alternative physiologically relevant states of the network producing similar phenotypic outcome.

To identify the minimal and sufficient set of reactants and their parameters (such as concentrations and reaction kinetics of their interactions) representing faithfully the behavior of a given network, the response of the computed system to perturbations therefore needs to be examined (Figs. 1C and 4A). For example, the concentration of one of the regulatory components of the model is varied and the response of other system components is evaluated. The application of a well-biochemically characterized and calibrated FRET-based sensor allows that similar experiments can be performed with the biological sample and the sensor-reported response can then be used to refine the computed model. Even in the case of the highly organized Ran-NTR system, it is initially advantageous to use an experimental model system devoid of the spatial anisotropy such as the cytoplasmic *Xenopus* egg extracts and to apply corresponding nondimensional computational models for the simulations. The response of the Ran-regulated importin β cargo release in *Xenopus laevis* egg extracts to biochemical perturbation is compared with the response of the computational mitotic Ran system model by varying the amount of free RanGTP (Fig. 4A).

As expected, in initial computed simulations, we found that the concentrations of transport receptors and their cargos, respectively, have a dominant effect on the

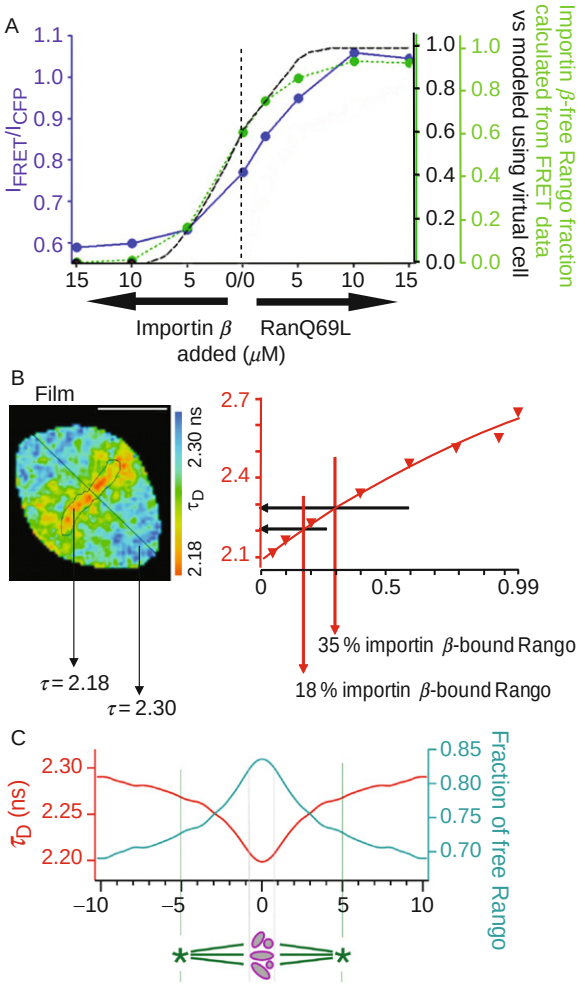

Fig. 4 (A) The response of the Ran-regulated importin β cargo release in *Xenopus laevis* egg extracts to biochemical perturbation, compared with the response of the computational mitotic Ran system model to simulated identical treatment. The amount of free RanGTP in the extracts was varied by adding increasing concentrations of RanQ69L or importin β. The Rango Förster (or fluorescence) resonance energy transfer (FRET) signal was measured as FRET intensity ratios (I_{FRET}/I_{CFP}, blue in color plate), and the corresponding fraction of importin β-free Rango calculated based on *in vitro* calibration (green in color plate). As the scales of the measured and calculated free Rango fraction nearly overlap, only the measured (green in color plate) scale is shown. Similarly, increasing concentrations of RanQ69L or importin β were added to a minimal computational mitotic Ran system containing Rango. The concentrations of the liberated Rango in the models were recorded upon reaching equilibrium (black). Note that the equilibrium conditions (0/0) in the extracts exhibit high sensitivity of importin β cargo liberation to small changes of RanGTP and importin β concentration. (B) The use of *in vitro* Rango fluorescence lifetime dose–response calibration to estimate the proportion of free versus importin β-bound Rango in live cells. The arrows indicate two points on the calibration curve corresponding to two selected areas in mitotic HeLa cell expressing Rango. (C) The average distribution

resulting Rango fractional occupancy at equilibrium. Next, we used Rango FRET measurements in mitotic *Xenopus* egg extracts to estimate the fraction of Rango bound to importin β at equilibrium. We used this measured fractional occupancy value (40% of Rango bound to importin β) to adjust the initial reactant concentrations in our computational model of Ran. After such adjustment (Table I), the response of our minimal computed Ran system model to simulated perturbations (addition of importin β and dominant RanGTP binding mutant, respectively) matched Rango occupancy values that were measured by FRET in the *Xenopus* egg extracts over a wide range of concentrations (Fig. 4). This liberation of Rango from importin β was quantitatively represented in our computer model. Importantly, the computed response of the minimal Ran-NTR system to RanGTP concentration validated the initially unexpected high concentration of free importin β cargos detected by FLIM in mitotic cells. Combined, the computational systems modeling and quantitative FLIM imaging in cells thus provided a fundamentally new important insight into the function of the mitotic RanGTP gradient. Instead of controlling SAFs as an on/off switch as previously hypothesized (Weis, 2003), the mitotic RanGTP gradient regulates spindle assembly by inducing local breaks in the symmetry between the cytoplasmic spindle assembly activators and inhibitors (Kalab and Heald, 2008; Kalab *et al.*, 2006).

E. Spatial Modeling and Protein Diffusion inside Cells

The refined nondimensional model validated by side-by-side *in vivo* and *in silico* perturbations is an excellent starting point for the construction of dimensional models. For example, in Virtual Cell, the model may be mapped on the actual 3D cellular geometry imported from microscopy images, including in the newest version reactions happening within the 2D cell membrane. Spatial symmetries in the model should be exploited to reduce the volume of computation. Often, 2D geometry can be found to sufficiently represent the 3D geometry.

In diffusion-limited reaction networks such as the mitotic Ran system, the particularly critical value influencing the outcome of the simulation is the diffusion rate of each model component. In the existing models of the Ran system, the diffusion of proteins inside cells was slowed down by an arbitrary factor relative to water to arrive at spatial dimensions of the measured Ran-regulated gradients (Caudron *et al.*, 2005). What are the factors defining diffusion of proteins in cells

---

of Rango fluorescence lifetime distribution measured in four mitotic HeLa cells (red line) was transformed to the corresponding distribution of the free Rango fraction (green line) calculated from the *in vitro* Rango calibration data [see (B) above]. This analysis revealed that ~68% cargos similar to Rango are importin β free at the cell periphery and ~86% importin β cargos are liberated at the peak of the RanGTP gradient at mitotic chromosomes, indicating that RanGTP gradient does not act as an of/off switch to regulate mitotic spindle assembly (Kalab and Heald 2008). The diameter of the free importin β cargo gradient is similar to the mitotic spindle size in HeLa cells (Kalab *et al.*, 2006)

Table I
Final Equilibrium Concentrations of the Components of the Minimal Computed Ran System

RanGTP	3 μM	RanBP	1.2 μM
RanGDP	3.6 μM	NTF2	0.6 μM
GDP	1.6 μM	Importin β	3 μM
GTP	470 μM	Importin β cargos	8 μM
RCC1	0.25 μM	Rango	2 μM
RanGAP	0.4 μM	Importin β-like transport receptors	5 μM

and how it is best described is a subject of intense research (Banks and Fradin, 2005; Petrasek and Schwille, 2007; Sanabria *et al.*, 2007; Verkman, 2002).

Detailed spatially resolved Ran systems models will require application of new developments in instrumentation, such as high speed FLIM imaging, such as spinning disk confocal FLIM (http://www.lambert-instruments.com/) and automated imaging in dividing cells (Pepperkok and Ellenberg, 2006) together with novel sensitive sensors for Ran function in cells.

V. Materials and Methods

A. Protein Expression and Purification

The plasmids for *E. coli* expression of Rango (pKW1648), IBB-Cerulean (pKW1648), EYFP-IBB (pKW1648), and ZZ-RanQ69L (pKW1234) were constructed in pRSET A (all with 6His tag) as described (Kalab *et al.*, 2006) and human importin β (pKW485) in pET30a (6His- S tag; Beresford *et al.*, 2001).

All proteins were expressed in BL21 DE3 *E. coli* cells. The cultures were inoculated with freshly transformed cells, grown until $OD_{600\ nm}$ 0.5–0.6 at 37 °C, transferred to room temperature shaker and induced with 0.3 mM IPTG. After 16-18 h, the cells were harvested by centrifugation, resuspended in ice-cold lysis buffer (PBS, 10 mM Imidazole, pH 7.4, 100 mM PMSF, 10μg/ml each of chymostatin, peptstatin, and leupeptin) and lysed by French pressure cell. The lysates were clarified (2 × 20 min, 15,000 rpm in Sorvall SS34), the 6His tagged proteins were batch bound to Ni-agarose beads (Qiagen or Sigma), and beads were washed on disposable plastic columns with the PBS, 10 mM Imidazol, pH 7.4. Proteins eluted with 0.2 M Imidazole, PBS were dialyzed overnight in XB (50 mM sucrose, 100 mM KCl, 0.1 mM $CaCl_2$, 1 mM $MgCl_2$, 10 mM HEPES, pH 7.7) and purified by gel filtration in XB buffer on FPLC on Separose 6 (Pharmacia). Absorbance at 435 and 512 nm was used to detect Cerulean and YFP and eliminate trailing fractions with partially inactivated fluorophores. Proteins were concentrated on Amicon 30 ultrafiltration colums (Millipore) to 100–200 μM, passed through 0.45 μm filter, snap-frozen in single use aliquots in liquid nitrogen and stored

at –80 °C. The protein concentration was measured with Bradford reagent (Pierce) using BSA as a standard and the purity of the proteins was assessed on SDS-PAGE with Coomassie Blue R250 staining. All fluorescent proteins expressed as soluble and typically we obtained ~10–20 mg of >95% pure protein/liter of culture.

B. Importin β-Rango Dissociation Constant

To obtain the apparent dissociation constant of Rango–importin β interaction, we monitored the importin β binding-induced loss of Rango I_{FRET}/I_{CFP} signal (Kalab *et al.*, 2006) in spectrofluorimeter. Aliquots of 40 nM Rango in PBS were diluted with increasing concentrations of importin β in PBS to achieve final concentration of 6 nM Rango and 0–40 nM importin β. The samples were placed in cuvettes, excited at 435 ± 2 nm and emission intensities at 474 nm (I_{CFP}) and 512 nm (I_{FRET}) was recorded. The I_{FRET}/I_{CFP} ratios were determined in two samples (2–3 scans each) from each dilution aliquot. The I_{FRET}/I_{CFP} values were plotted against the importin β concentration and data were fitted with a down to bottom curve, standard slope using GraphPad Prism version 4.00 for Windows (GraphPad Software, San Diego, CA). The Rango–importin β dissociation constant was determined using the importin β concentration at 50% amplitude of Rango I_{FRET}/I_{CFP} curve.

C. HeLa Cell Culture

Adherent HeLa cells were obtained from ATCC and maintained in 75 cm^2 flat bottom flasks at 37 °C, 5% CO_2. After the first two passages in DMEM (Gibco, Invitrogen) with 10% FBS, the cells were transferred to culture in Opti-MEM (Gibco, Invitrogen) with 4% FBS by increasing the proportion of the new media by 1/3 in each passage. New passages were initiated before reaching confluency (confluency: ~10 × 10^6cells/75 cm^2 flask). The cells were lifted with Trypsin-Versene (Gibco, Invitrogen), thoroughly resuspended, and 1/4–1/5 cells seeded into a new flask containing 11 ml media equilibrated in the incubator.

D. Monoclonal HeLa Cell Culture

To obtain single-cell derived cell cultures, dispersed ATCC HeLa cells were plated at ~200 cells per 9 cm diameter tissue culture dish and kept in culture for 4–5 weeks while regularly exchanging the media. Colonies displaying good growth were marked on the bottom of the dish. The medium from the plate was removed and few cells were picked from the marked colonies with plastic pipette tips and seeded into individual 24-well plates containing 0.1 ml Trypsine-Versene (Gibco-BRL)/well. The cells were dispersed by pipetting and 0.5 ml serum containing media was added. Well-growing colonies were identified and used for second round of single colony selection. Three selected cell lines were amplified in 75 cm^2 flasks and frozen in multiple aliquots from their first and second passages. Cells used for FLIM experiments underwent at most 15 passages.

E. Glass Cover Slides for Cell Culture

Round cover glass (25 mm diameter, Fisher Scientific) used for live cell imaging was cleaned using modified acid wash protocol (Salmon lab: www.bio.unc.edu/faculty/salmon/lab/). The slides were first soaked in 1 M HCl at 65 °C overnight. After a thorough rinse with distilled and deionized water (ddH_2O), slides placed in 100-ml screw cap covered bottles were sonicated on water bath for 30min. The sonication in ddH_2O was repeated two more times followed with 30-min sonication each in 50, 60, 70, 80, 90, and twice in 100% ethanol (Gold Shield, Rossville Alcohol). In order to remove any residues, the ethanol was burnt from the slides in a gas burner flame in sterile tissue culture hood just before the slides were used for seeding cells.

F. Preparation of Cells for Live Cell Imaging

Two to four days before the experiment, cells were seeded from sub-confluent cultures to 6-well plates containing 25 mm round glass slides/well, at two concentrations: 2×10^4 and at 5×10^4cells/well. Sixteen to 24h later, the cells were transfected with the FRET probes using Fugene 6 (Roche Pharmaceuticals) according to the protocol of the manufacturer. Cells plated at higher concentration were used for FLIM at least 20–24h following the transfection. The cells plated at the lower density were typically suitable for microscopy 4 days since the start of the culture.

We tested several media for imaging and found that high FBS concentration and Phenol Red induced short-lifetime background in FLIM in our conditions (absence of enclosed environmental chamber on the microscope stage). The best results were obtained with Dulbecco's PBS (Gibco, Invitrogen) supplemented with 1mM sodium pyruvate (Gibco, Invitrogen) (Kalab *et al.*, 2006) although also DMEM without Phenol Red (Cellgro), 4% FBS was acceptable. For live cell imaging experiments, cells were maintained at 30 °C in a temperature controlled imaging chamber (Warner instruments). The bottom of the imaging chamber was formed directly with the 25 mm round glass with cells taken from the culture just before imaging. The cells were gently rinsed once with the imaging media and the microscopy was performed within the next 60–90 min.

G. Spectrophotometry

Emission spectra were analyzed with a Fluorolog 2spectrofluorimeter controlled by Datamax 2.2 (Jobin Yvon Spex) and the Grams 3.04 II software package (Galactic Industries, Salem, NH).

H. Imaging Conditions Used in the Rango FLIM Study

The FLIM data in the Rango study (Kalab *et al.*, 2006) were acquired on an inverted Zeiss LSM510 Axiovert 200M microscope with a NeoFLUAR 40 × 1.3 NA oil-immersion objective lens, equipped with a TCSPC controller (Becker &

Hickl SPC-730 card). Samples were excited by 6 μW of 435 nm laser light generated by frequency-doubling (Pulse-Selector 3980, SpectraPhysics, USA) the 870 nm pulses from a mode-locked Ti:Sapphire laser (Tsunami, SpectraPhysics, 120–150 fs pulse width, 80 MHz repetition rate). The pulse length and shape of the Ti:Sapphire laser were adjusted to provide maximum conversion to blue light. The 435 nm pulses were filtered by a 435BP40 filter, merged with the light from a 532-nm laser used to excite Rhodamine-labeled tubulin, and coupled via a single-mode fiber (PointSource, UK) into the scanhead of the Zeiss LSM510. The emission light was filtered with a 480-nm bandpass filter (480BP40, Chroma) and detected by a PMC-100 photomultiplier (Becker & Hickl) coupled to the fiber-out port of the LSM510. Images of 64 $\times$ 64 pixels or 128 $\times$ 128 pixels were acquired over 1–4 min.

I. FLIM Image Analysis: Fitting TCSPC Data to Obtain a Lifetime

Each decay curve is fitted to obtain the lifetime(s) in that image point. The Rango FLIM date was analyzed off-line using pixel-based fitting software (SPCImage, Becker & Hickl), assuming single exponential incomplete decay during the 12.5 ns interval between laser pulses.

To obtain the correct fluorescence lifetime, the time that it takes for the light to travel from the laser to the sample and then from the sample to the detector has to be known. This instrument-specific variable is called *instrument response (IR) function* of the microscope and limits the shortest measurable lifetimes. Usually, the IR is either measured with a reflecting sample or may be fitted from the shape of lifetime data obtained from a fluorescent sample.

J. Statistical Analysis

Statistical analyses were performed with Excel (Microsoft) and with GraphPad Prism version 4.00 for Windows, GraphPad Software (www.graphpad.com).

K. Computational Modeling

The computational model of a minimal Ran system coupled to the minimal set of nuclear transport receptors, including importin β and Rango, was built using Virtual Cell (www.vcell.org/index.html). The kinetic parameters that we applied have been described previously (Gorlich *et al.*, 2003; Riddick and Macara, 2005).

References

Alves, R., Antunes, F., and Salvador, A. (2006). Tools for kinetic modeling of biochemical networks. *Nat. Biotechnol.* **24,** 667–672.

Banks, D., and Fradin, C. (2005). Anomalous diffusion of proteins due to molecular crowding. *Biophys. J.* **89,** 2960–2971.

Bastiaens, P., Caudron, M., Niethammer, P., and Karsenti, E. (2006). Gradients in the self-organization of the mitotic spindle. *Trends Cell Biol.* **16,** 125–134.

Becker, W., Bergmann, A., Hink, M. A., Konig, K., Benndorf, K., and Biskup, C. (2004). Fluorescence lifetime imaging by time-correlated single-photon counting. *Microsc. Res. Technol.* **63,** 58–66.

Beresford, P., Zhang, D., Oh, D., Fan, Z., Greer, E., Russo, M., Jaju, M., and Lieberman, J. (2001). Granzyme A activates an endoplasmic reticulum-associated caspase-independent nuclease to induce single-stranded DNA nicks. *J. Biol. Chem.* **276,** 43285–43293.

Bird, D. K., Yan, L., Vrotsos, K. M., Eliceiri, K. W., Vaughan, E. M., Keely, P. J., White, J. G., and Ramanujam, N. (2005). Metabolic mapping of MCF10A human breast cells via multiphoton fluorescence lifetime imaging of the coenzyme NADH. *Cancer Res.* **65,** 8766–8773.

Bustamante, C., Marko, J., Siggia, E., and Smith, S. (1994). Entropic elasticity of lambda-phage DNA. *Science* **265,** 1599–1600.

Caudron, M., Bunt, G., Bastiaens, P., and Karsenti, E. (2005). Spatial coordination of spindle assembly by chromosome-mediated signaling gradients. *Science* **309,** 1373–1376.

Chorvat, D., Jr., and Chorvatova, A. (2006). Spectrally resolved time-correlated single photon counting: A novel approach for characterization of endogenous fluorescence in isolated cardiac myocytes. *Eur. Biophys. J.* **36,** 73–83.

Cingolani, G., Petosa, C., Weis, K., and Muller, C. W. (1999). Structure of importin-beta bound to the IBB domain of importin-alpha. *Nature* **399,** 221–229.

Clegg, R. M. (1966). "Fluorescence Resonance Energy Transfer." Wiley, New York.

Denk, W., Strickler, J. H., and Webb, W. W. (1990). Two-photon laser scanning fluorescence microscopy. *Science* **248,** 73–76.

Denk, W., and Svoboda, K. (1997). Photon upmanship: Why multiphoton imaging is more than a gimmick. *Neuron* **18,** 351–357.

Erickson, M. G., Alseikhan, B. A., Peterson, B. Z., and Yue, D. T. (2001). Preassociation of calmodulin with voltage-gated Ca^{2+} channels revealed by FRET in single living cells. *Neuron* **31,** 973–985.

Evers, T. H., van Dongen, E. M., Faesen, A. C., Meijer, E. W., and Merkx, M. (2006). Quantitative understanding of the energy transfer between fluorescent proteins connected via flexible peptide linkers. *Biochemistry* **45,** 13183–13192.

Förster, T. (1946). Energiewanderung und Fluoreszenz. *Naturwissenschaften* **6,** 166–175.

Förster, T. (1948). Zwischenmoleculare Energiewanderung und Fluoreszenz (Inter-molecular energy migration and fluorescence). *Annalen der Physik* **2,** 55–75.

Ganesan, S., Ameer-Beg, S. M., Ng, T. T., Vojnovic, B., and Wouters, F. S. (2006). A dark yellow fluorescent protein (YFP)-based resonance energy-accepting chromoprotein (REACh) for Forster resonance energy transfer with GFP. *Proc. Natl. Acad. Sci. USA* **103,** 4089–4094.

Giepmans, B. N., Adams, S. R., Ellisman, M. H., and Tsien, R. Y. (2006). The fluorescent toolbox for assessing protein location and function. *Science* **312,** 217–224.

Gordon, G. W., Berry, G., Liang, X. H., Levine, B., and Herman, B. (1998). Quantitative fluorescence resonance energy transfer measurements using fluorescence microscopy. *Biophys. J.* **74,** 2702–2713.

Gorlich, D., Seewald, M. J., and Ribbeck, K. (2003). Characterization of Ran-driven cargo transport and the RanGTPase system by kinetic measurements and computer simulation. *EMBO J.* **22,** 1088–1100.

Gruss, O. J., and Vernos, I. (2004). The mechanism of spindle assembly: Functions of Ran and its target TPX2. *J. Cell Biol.* **166,** 949–955.

Helmchen, F., and Denk, W. (2002). New developments in multiphoton microscopy. *Curr. Opin. Neurobiol.* **12,** 593–601.

Hetzer, M., Gruss, O. J., and Mattaj, I. W. (2002). The Ran GTPase as a marker of chromosome position in spindle formation and nuclear envelope assembly. *Nat. Cell Biol.* **4,** E177–E184.

Johnsson, N., and Johnsson, K. (2007). Chemical tools for biomolecular imaging. *ACS Chem. Biol.* **2,** 31–38.

Jung, G., Wiehler, J., and Zumbusch, A. (2005). The photophysics of green fluorescent protein: Influence of the key amino acids at positions 65, 203, and 222. *Biophys. J.* **88,** 1932–1947.

Kajihara, D., Abe, R., Iijima, I., Komiyama, C., Sisido, M., and Hohsaka, T. (2006). FRET analysis of protein conformational change through position-specific incorporation of fluorescent amino acids. *Nat. Methods* **3,** 923–929.

Kalab, P., and Heald, R. (2008). The RanGTP gradient – A GPS for the mitotic spindle. *J. Cell Sci.* **121,** 1577–1586.

Kalab, P., Pralle, A., Isacoff, E. Y., Heald, R., and Weis, K. (2006). Analysis of a RanGTP-regulated gradient in mitotic somatic cells. *Nature* **440,** 697–701.

Kalab, P., Weis, K., and Heald, R. (2002). Visualization of a Ran-GTP gradient in interphase and mitotic *Xenopus* egg extracts. *Science* **295,** 2452–2456.

Kitano, H. (2002). Computational systems biology. *Nature* **420,** 206–210.

Kollner, M., and Wolfrum, J. (1992). How many photons are necessary for fluorescence-lifetime measurements. *Chem. Phys. Lett.* **200,** 199–204.

Lakowicz, J. R. (1999). ''Principles of Fluorescence Spectroscopy,'' 2nd edn. Plenum, New York.

Lakowicz, J. R., Szmacinski, H., Nowaczyk, K., and Johnson, M. L. (1992). Fluorescence lifetime imaging of free and protein-bound NADH. *Proc. Natl. Acad. Sci. USA* **89,** 1271–1275.

Mitra, R. D., Silva, C. M., and Youvan, D. C. (1996). Fluorescence resonance energy transfer between blue-emitting and red-shifted excitation derivatives of the green fluorescent protein. *Gene* **173,** 13–17.

Miyawaki, A., Griesbeck, O., Heim, R., and Tsien, R. Y. (1999). Dynamic and quantitative Ca^{2+} measurements using improved cameleons. *Proc. Natl. Acad. Sci. USA* **96,** 2135–2140.

Monici, M. (2005). Cell and tissue autofluorescence research and diagnostic applications. *Biotechnol. Annu. Rev.* **11,** 227–256.

Nguyen, A. W., and Daugherty, P. S. (2005). Evolutionary optimization of fluorescent proteins for intracellular FRET. *Nat. Biotechnol.* **23,** 355–360.

Niethammer, P., Bastiaens, P., and Karsenti, E. (2004). Stathmin-tubulin interaction gradients in motile and mitotic cells. *Science* **303,** 1862–1866.

Ohashi, T., Galiacy, S. D., Briscoe, G., and Erickson, H. P. (2007). An experimental study of GFP-based FRET, with application to intrinsically unstructured proteins. *Protein Sci.* **16,** 1429–1438.

Owen, D. M., Auksorius, E., Manning, H. B., Talbot, C. B., de Beule, P. A. A., Dunsby, C., Neil, M. A. A., and French, P. M. W. (2007). Excitation-resolved hyperspectral fluorescence lifetime imaging using a UV-extended super-continuum source. *Opt. Lett.* **32,** 3408–3410.

Pemberton, L. F., and Paschal, B. M. (2005). Mechanisms of receptor-mediated nuclear import and nuclear export. *Traffic* **6,** 187–198.

Peter, M., Ameer-Beg, S. M., Hughes, M. K., Keppler, M. D., Prag, S., Marsh, M., Vojnovic, B., and Ng, T. (2005). Multiphoton-FLIM quantification of the EGFP-mRFP1 FRET pair for localization of membrane receptor-kinase interactions. *Biophys. J.* **88,** 1224–1237.

Pepperkok, R., and Ellenberg, J. (2006). High-throughput fluorescence microscopy for systems biology. *Nat. Rev. Mol. Cell Biol.* **7,** 690–696.

Petrasek, Z., and Schwille, P. (2007). Precise measurement of diffusion coefficients using scanning fluorescence correlation spectroscopy. *Biophys. J.* **94,** 1437–1448.

Philip, J., and Carlsson, K. (2003). Theoretical investigation of the signal-to-noise ratio in fluorescence lifetime imaging. *J. Opt. Soc. Am. A Opt. Image Sci. Vis.* **20,** 368–379.

Remington, S. J. (2006). Fluorescent proteins: Maturation, photochemistry and photophysics. *Curr. Opin. Struct. Biol.* **16,** 714–721.

Riddick, G., and Macara, I. G. (2005). A systems analysis of importin-α-β mediated nuclear protein import. *J. Cell Biol.* **168,** 1027–1038.

Rizzo, M. A., Springer, G. H., Granada, B., and Piston, D. W. (2004). An improved cyan fluorescent protein variant useful for FRET. *Nat. Biotechnol.* **22,** 445–449.

Sanabria, H., Kubota, Y., and Waxham, M. (2007). Multiple diffusion mechanisms due to nanostructuring in crowded environments. *Biophys. J.* **92,** 313–322.

Shimozono, S., Hosoi, H., Mizuno, H., Fukano, T., Tahara, T., and Miyawaki, A. (2006). Concatenation of cyan and yellow fluorescent proteins for efficient resonance energy transfer. *Biochemistry* **45,** 6267–6271.

Shu, X., Shaner, N. C., Yarbrough, C. A., Tsien, R. Y., and Remington, S. J. (2006). Novel chromophores and buried charges control color in fruits. *Biochemistry* **45,** 9639–9647.

Slepchenko, B. M., Schaff, J. C., Macara, I., and Loew, L. M. (2003). Quantitative cell biology with the virtual cell. *Trends Cell Biol.* **13,** 570–576.

Skala, M. C., Riching, K. M., Bird, D. K., Gendron-Fitzpatrick, A., Eickhoff, J., Eliceiri, K. W., Keely, P. J., and Ramanujam, N. (2007). *In vivo* multiphoton fluorescence lifetime imaging of protein-bound and free nicotinamide adenine dinucleotide in normal and precancerous epithelia. *J. Biomed. Opt.* **12**, 024014.

Smith, A. E., Slepchenko, B. M., Schaff, J. C., Loew, L. M., and Macara, I. G. (2002). Systems analysis of Ran transport. *Science* **295,** 488–491.

Suhling, K., French, P. M., and Phillips, D. (2005). Time-resolved fluorescence microscopy. *Photochem. Photobiol. Sci.* **4,** 13–22.

Tramier, M., Zahid, M., Mevel, J. C., Masse, M. J., and Coppey-Moisan, M. (2006). Sensitivity of CFP/YFP and GFP/mCherry pairs to donor photobleaching on FRET determination by fluorescence lifetime imaging microscopy in living cells. *Microsc. Res. Tech.* **69,** 933–939.

Tsien, R. Y. (1998). The green fluorescent protein. *Annu. Rev. Biochem.* **67,** 509–544.

Tsien, R. Y. (2003). Breeding molecules to spy on cells. *Harvey Lect.* **99,** 77–93.

Tsien, R. Y. (2006). Breeding and building molecules to spy on cells and tumors. *Keio J. Med.* **55,** 127–140.

Tsien, R. Y., Backsai, B. J., and Adams, S. R. (1993). FRET for studying intracellular signalling. *Trends Cell Biol.* **3,** 242–245.

van Munster, E. B., and Gadella, T. W. (2005). Fluorescence lifetime imaging microscopy (FLIM). *Adv. Biochem. Eng. Biotechnol.* **95,** 143–175.

Verkman, A. (2002). Solute and macromolecule diffusion in cellular aqueous compartments. *Trends Biochem. Sci.* **27,** 27–33.

Wang, L., and Tsien, R. Y. (2006). Evolving proteins in mammalian cells using somatic hypermutation. *Nat. Protoc.* **1,** 1346–1350.

Weis, K. (2003). Regulating access to the genome: Nucleocytoplasmic transport throughout the cell cycle. *Cell* **112,** 441–451.

Yasuda, R. (2006). Imaging spatiotemporal dynamics of neuronal signaling using fluorescence resonance energy transfer and fluorescence lifetime imaging microscopy. *Curr. Opin. Neurobiol.* **16,** 551–561.

Yasuda, R., Harvey, C. D., Zhong, H., Sobczyk, A., van Aelst, L., and Svoboda, K. (2006). Supersensitive Ras activation in dendrites and spines revealed by two-photon fluorescence lifetime imaging. *Nat. Neurosci.* **9,** 283–291.

Zacharias, D. A., and Tsien, R. Y. (2006). Molecular biology and mutation of green fluorescent protein. *Methods Biochem. Anal.* **47,** 83–120.